Research Article Vol. 7, No. 12 / December 2020 / Optica 1673

optica

Dynamically tuned arrays of polariton parametric oscillators

Alexander S. Kuznetsov,[1,*] Galbadrakh Dagvadorj,[2,3] Klaus Biermann,[1] Marzena H. Szymanska,[3] and Paulo V. Santos[1]

[1]Paul-Drude-Institut für Festkörperelektronik, Leibniz-Institut im Forschungsverbund Berlin e. V., 5-7 Hausvogteiplatz, Berlin, 10117, Germany
[2]Department of Physics, University of Warwick, Coventry CV4 7AL, UK
[3]Department of Physics and Astronomy, University College London, Gower St, Kings Cross, London WC1E 6BT, UK
*Corresponding author: kuznetsov@pdi-berlin.de

Received 8 June 2020; revised 20 October 2020; accepted 26 October 2020 (Doc. ID 399747); published 23 November 2020

Optical parametric oscillations (OPOs)—the nonlinear coherent coupling of an optically excited two-particle pump state to signal and idler states correlated in energy—is relevant for optical amplification and generation of correlated photons. OPOs require states with well-defined symmetries and energies; the fine-tuning of material properties and structural dimensions remains a challenge for the realization of scalable OPOs in semiconductor nanostructures. Here we demonstrate a pathway towards arrays of OPOs based on the dynamic control of microcavity exciton-polaritons confined in micrometer-sized intracavity traps by an acoustic wave. The spatially varying strain field of the wave induces state-dependent energy shifts of discrete polariton levels with the appropriate symmetry for OPO triggering. The robustness of the dynamic acoustic tuning is demonstrated by the synchronous excitation of an array of confined OPOs using a single wave, which thus opens the way for the realization of scalable nonlinear on-chip systems.

https://doi.org/10.1364/OPTICA.399747

1. INTRODUCTION

Many fundamental physical concepts developed for atoms can be conveniently emulated by confined solid-state systems with discrete energy levels. Unlike real atoms, these solid-state analogues suffer from disorder associated with fluctuations in material properties and structural dimensions, which impair their implementation as well as their exploitation for complex and scalable solid-state functionalities. Particularly challenging examples are nonlinear functionalities such as optical parametric oscillations (OPOs) and amplification (OPA), which are technologically relevant for signal processing as well as for the generation of correlated photon states. These functionalities rely on the coherent coupling of multiple confined states with well-defined energies and symmetries, which is presently difficult to implement in solid-state structures. This paper introduces a pathway to overcome these limitations based on the fine-tuning of confined states using dynamic acoustic fields.

Studies were carried out using confined states of microcavity exciton-polaritons (polaritons)—light-matter quasi-particles resulting from the strong coupling between quantum well (QW) excitons and photons in a semiconductor microcavity (MC) [1]. Strong interparticle interactions and long spatial coherence of polaritons bring the rich physics of correlated systems to an all-semiconductor platform [2,3]. Owing to their bosonic nature, polaritons undergo condensation at high particle densities [4]. Combined with the peculiar shape of the polariton energy dispersion, polariton properties enable OPOs [5–7] as well as OPA with very large gain [6,8]. Here, two pump (p) polaritons, resonantly excited at the inflection point of the dispersion, scatter into a signal (s) at the bottom of the dispersion state and a higher lying idler (i) state while conserving energy and momentum [9–12]. This resonant scheme generates correlated idler–signal polariton pairs; it has been applied to multiple cavity structures [13] as well as for the direct excitation of Bose–Einstein condensates of polaritons [5].

Owing to their large de Broglie wavelength, polaritons can be confined within micrometer (μm)-scale traps, which thus opens the way for the control of their properties using structural dimensions [14]. The discrete levels of a trap can act as pump, signal, and idler states of an OPO, provided that they have the proper energy and symmetry matching [15]. This approach profits from the enhanced nonlinearities due to the high density of polaritons that can be excited in confined potentials. In addition, it can be scaled for the realization of OPO arrays with correlated emission properties. OPOs in traps require, however, a very high degree of control of the confinement potential. Despite significant recent progress [15–17], the realization of confined OPOs remains a challenging task, which has so far only been achieved in single, isolated structures. The realization of an OPO lattice, which is presently hindered by inhomogeneities and the limited degree of

control of polariton potential landscape, represents, therefore, a major technological milestone.

In this work, we introduce a robust approach for the realization of arrays of polariton OPOs via the tuning of confined polariton states by the spatially and time-varying dynamical potentials of a surface acoustic wave (SAW). The studies are carried out in arrays of intracavity polariton traps defined in the spacer layer of an (Al, Ga)As MC [18]. The array is placed within an acoustic resonator defined by two opposing interdigitated piezoelectric transducers (IDTs) with the array sites located on the antinodes of the standing acoustic field as illustrated in Fig. 1(a). In the absence of the acoustic excitation, the energy configuration of the trap levels does not fulfill the conditions for the OPO excitation as illustrated schematically by the dashed lines in Fig. 1(b). In contrast, under the acoustic field, the optical pumping of the confined state Φ_{21} triggers OPOs at all sites of the array as shown by the spectral photoluminescence (PL) map of Fig. 1(c) (see further details in Section 3.C on OPO arrays).

2. METHODS

A. Sample

Confined polariton states originate from μm-sized intracavity traps defined within the spacer layer of an (Al, Ga)As MC. The traps were produced by etching the spacer layer of the MC between growth steps by molecular beam epitaxy (MBE). The sample was grown on a GaAs (001) substrate with the structure schematically illustrated in Fig. 1(a). During the MBE growth run, the lower distributed Bragg reflector (DBR) and the MC spacer region containing three pairs of 15 nm thick GaAs QWs centered at the antinodes of the optical field were deposited and then terminated by a 120 nm thick $Al_{0.15}Ga_{0.85}$ As layer. The sample was then removed from the MBE chamber and patterned by means of photolithography and wet chemical etching to form 12 nm high and a few-μm-wide mesas with different shapes. For the final growth step, the sample was reinserted in the MBE chamber for the deposition of the upper DBR. The lower and upper DBRs consist of 58.7 nm and 65.8 nm thick pairs of $Al_{x_1}Ga_{1-x_1}As/Al_{x_2}Ga_{1-x_2}As$ with different Al compositions $x_1 = 0.15$ and $x_2 = 0.75$.

The etching of the MC spacer layer results in a blueshift of the bare optical mode of the MC by 9 meV. As a consequence, the energy of the lower polariton mode in the etched regions is approximately $E_b = 5.5$ meV higher than in the nonetched areas. Polariton traps with an energy barrier E_b can then be formed by enclosing a μm-sized nonetched region by etched areas. Due to the conformal nature of the MBE growth, the lateral dimensions of the traps can be determined by measuring the surface relief of the MC. The anisotropic MBE overgrowth yields traps with different profiles along the trap sides oriented along the $x = [\bar{1}10]$ and $y = [\bar{1}\bar{1}0]$ surface directions. A detailed analysis of atomic force microscopy profiles from the traps presented in Section 1 of Supplement 1 shows that the confinement potential is mirror symmetric with respect to vertical planes $x = 0$ and $y = 0$ but with different profiles along the two directions.

B. Spectroscopy

The spectroscopic studies were performed at a temperature between 6 and 10 K in an optical cryostat with radio-frequency (rf) feedthroughs for the excitation of SAWs. A continuous-wave (cw) laser beam from a cavity-stabilized tunable Ti-sapphire laser was focused on the sample to a spot of approximately 50 μm. An objective with 3 cm diameter and 5 cm focal distance was used for the focusing of the excitation and for collecting the PL. In order to control the angle of incidence, the laser beam with approximately 3 mm diameter was incident on the objective at normal incidence and with a precisely controlled variable offset with respect to its center. The offset results in the change of the angle of incidence of the focused beam. The incident laser power could be varied in a broad range from a few microwatts (μW)to hundreds of milliwatts (mW). The angle of incidence of the laser (10°) was chosen to match the emission peak in momentum space of the Ψ_{21} state [cf. Fig. 2(a)]. In addition, this configuration helps to avoid the specular reflection of the pump. Due to focusing, the excitation beam has an angular spread of ±2°. The momentum-resolved PL

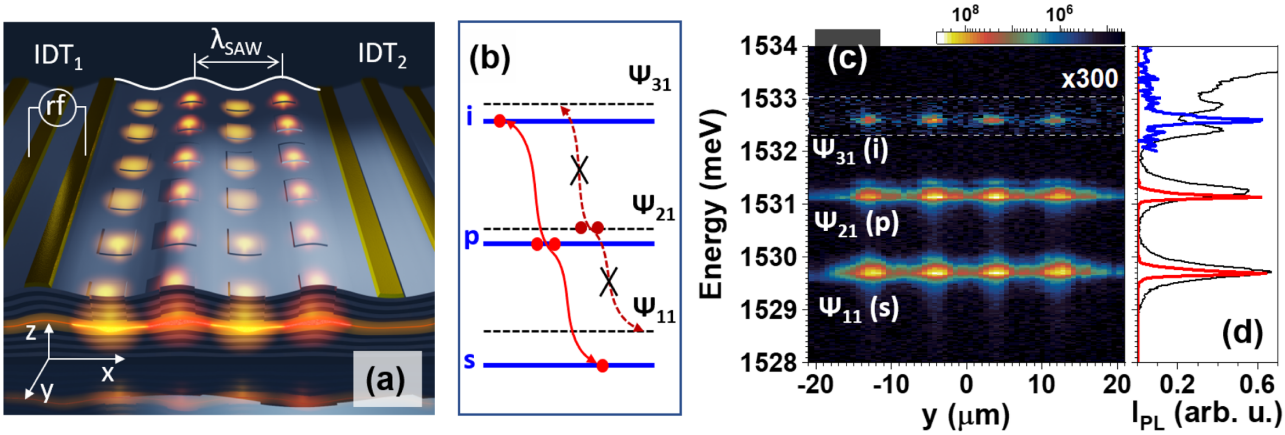

Fig. 1. SAW-induced arrays of OPOs. (a) Acoustic modulation of an array of intracavity polariton traps. The traps are positioned at the antinodes of the standing field of an acoustic resonator consisting of a driving interdigital transducer (IDT_1) and a passive, reflecting one (IDT_2). (b) A sketch of confined levels of a single trap in the absence (dashed line) and under a SAW (solid lines). The SAW induces level-dependent energy shifts that enable an OPO where two pump polaritons injected at the pump state (p, Ψ_{21}) scatter into equidistantly spaced signal (s, Ψ_{11}) and idler (i, Ψ_{31}) states. (c) Photoluminescence (PL) mapping of a row of traps of the OPO array. The array consists of nominally 3×3 μm^2 intracavity traps with a pitch of 9 μm resonantly excited in Ψ_{21}. The signal and idler states are designated as Ψ_{11} and Ψ_{31}, respectively. (d) The black line corresponds to the spatially integrated PL spectrum of a single trap recorded under weak nonresonant excitation. The red and blue curves are integrated PL of the second from the left trap in (c). The red curve was divided by 2×10^9 and the blue one by 4.4×10^6.

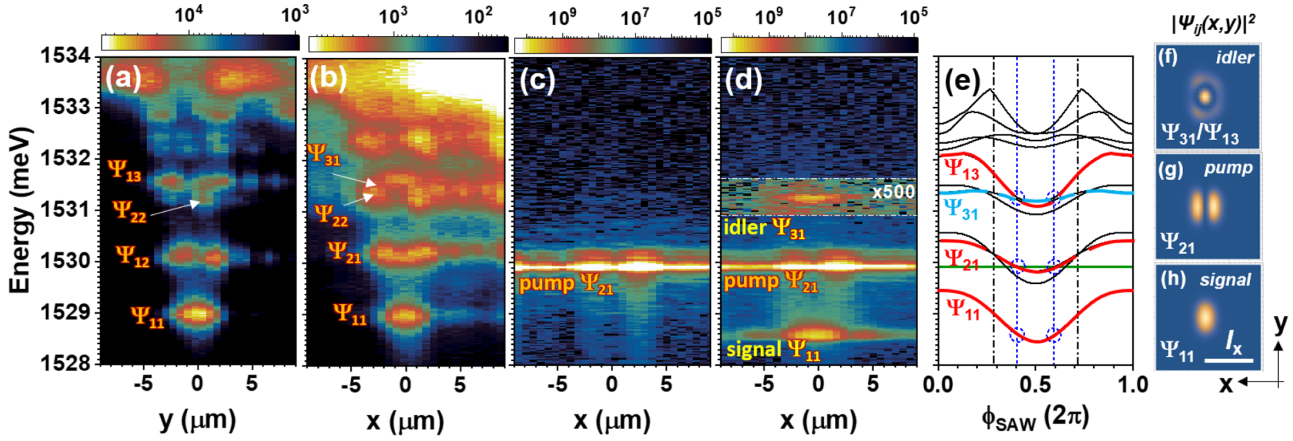

Fig. 2. OPO in a polariton trap with redshifted pump. Photoluminescence maps of the squared wave functions $|\Psi_{ij}|^2$ $(i, j = 1, 2, 3)$ of confined polariton levels in a 4×4 μm^2 intracavity trap projected on the (a) $y = 0$ and (b) $x = 0$ planes under the low-density, nonresonant optical excitation. (c)–(d) The corresponding spatially resolved PL maps recorded under quasi-resonant excitation of the Ψ_{21} confined level in the (c) absence and (d) presence of a standing SAW along the x direction. (e) Calculated energy evolution of the confined levels $\Psi_{m_x m_y}$ with the SAW phase ϕ_{SAW}: the labeled ones (thick red curves) are levels of the OPO set $O_2 = \{\Psi_{11}, \Psi_{21}, \Psi_{31}/\Psi_{13}\}$. The dash-dotted black vertical lines designate SAW phase for which the levels correspond to the unmodulated ones. The green horizontal solid line marks the pump energy, while the vertical dashed blue lines show the phases of equidistant separation between the levels within O_2. (f)–(h) Calculated $|\Psi_{m_x m_y}(x, y)|^2$ projections on the $x - y$ plane corresponding to the $\phi_{\mathrm{SAW}} = 0.415(2\pi)$.

was collected for angles between 0° and ±16° with respect to the sample surface.

Time-resolved studies of the OPO dynamics were carried out by detecting the PL with a streak camera synchronized with the rf signal used to excite the SAW resonator.

C. Acoustics

For acoustic excitation, we used a SAW delay line formed by two single-finger interdigital transducers (IDTs). The latter were designed for launching SAWs along the $x||[\bar{1}10]$ surface direction with a wavelength of 8 μm (corresponding to an acoustic frequency $f_{\mathrm{SAW}} = 383.66$ MHz at 10 K). Only one of the two IDTs was rf driven. The other acted as a passive acoustic reflector. The delay line forms an acoustic resonator with a quality factor of 4700 [19]. Care was taken to match the location of the traps with the antinodes of the SAW strain field.

3. RESULTS

A. SAW-Induced OPO

Figures 2(a) and 2(b) compare PL maps of a square trap with nominal dimensions of 4×4 μm^2 projected on the $x = 0$ and $y = 0$ planes, respectively. These maps were recorded under low-density nonresonant optical excitation by collecting the PL with spatial resolution along two perpendicular directions, which thus yielded the projection of the squared wave functions $|\Psi_{ij}|^2$ $(i, j = 1, 2, \ldots)$ of the confined polariton levels on the $x = 0$ and $y = 0$ axes, respectively. The i and j indices denote the number of lobes of $|\Psi_{ij}|^2$ along the x and y directions, respectively.

The polariton states in the intracavity traps can be approximated by those of a rectangular one with infinite barriers and dimensions $\ell_x \sim \ell_y$ along the x and y directions, respectively, which can be classified by indices (m_x, m_y), $m_i = 1, 2, \ldots$ and $i = x, y$ according to

$$E_{m_x m_y} = E_{\mathrm{LP}} + \frac{\hbar^2}{2m_p}\left[\left(\frac{m_x - 1}{l_x}\right)^2 + \left(\frac{m_y - 1}{l_y}\right)^2\right]. \quad (1)$$

Here $\hbar$ is Planck's constant, m_p is the reduced polariton mass, and is E_{LP} the lower polariton energy in the absence of the lateral confinement. The corresponding wave functions can be written as

$$\Psi_{m_x m_y}(x, y) = \frac{\sqrt{(k_x k_y)}}{\pi} \times \left[\cos\left(m_x k_x x + (m_x - 1)\frac{\pi}{2}\right) \times \cos\left(m_y k_y y + (m_y - 1)\frac{\pi}{2}\right)\right], \quad (2)$$

with $k_i = \pi/\ell_i$. Note that the wave function projections in Figs. 2(a) and 2(b) do not show modes with nodes on the y or x axis, respectively. As a consequence, some of the modes are either very weak or simply do not appear in the maps [one example is the Ψ_{22} mode displayed in Fig. S1(i)].

According to Eq. (1), the confined levels with the set $\{\Psi_{\mathrm{signal}}, \Psi_{\mathrm{pump}}, \Psi_{\mathrm{idler}}\} = O_1 = \{\Psi_{11}, \Psi_{12}$ or $\Psi_{21}, \Psi_{22}\}$ are equidistant in energy for $\ell_x = \ell_y$, which thus satisfyies the energy requirements for OPOs. The lowest three confined levels in Fig. 2(a), however, do not follow this behavior. In addition, the levels Ψ_{12} and Ψ_{21} are not degenerate; cf. Figs. 2(a) and 2(b). These discrepancies arise from the deviation of the realized confinement potential from a perfect square shape due to the anisotropic effects during the MBE overgrowth (cf. Supplement 1 Section 1 for details). The impact of the anisotropic shape on the confined states can be reproduced by assuming $\ell_x \neq \ell_y$ in Eq. (1), which lifts the degeneracy of the (m_x, m_y) and (m_y, m_x) states with $(m_x \neq m_y)$.

The energy spacing is dictated by the energy spectrum of the modes confined in the polariton trap. These energy levels depend on the lithographically defined lateral dimensions of the trap and on the height of the potential barrier. The latter can be controlled by the physical height of the mesa structures defined in the microcavity spacer.

The different interlevel spacings and the symmetry of the states (cf. Section 4.B) within O_1 prevent OPO excitation by optically

pumping the Ψ_{21} level. An experimental implementation is illustrated in the PL map of Fig. 2(c). Here the trap was illuminated by a cw laser beam slightly redshifted with respect to the Ψ_{21} emission in Figs. 2(a)–2(b), but within its linewidth. The angle of incidence of the laser was chosen to match the emission peak in the momentum space of the Ψ_{21} state. Indeed, in the case of the resonant excitation [cf. Fig. 2(c)], one should match the angle of incidence of the excitation with the angular (momentum) distribution of the level. There is a correspondence between the real space and momentum space as shown in Fig. 3. Hence, state Ψ_{21}, with two lobes along the x direction [see Fig. 2(b)], will have two lobes in the momentum space; cf. Fig. 6(a). In our configuration, the x-momentum values of $k_x = \pm 1.4\ \mu\text{m}^{-1}$ correspond to the emission angle of $\pm 10°$. Therefore, the excitation angle was set to the same value. Figure 2(c) shows a slight increase of the Rayleigh scattering due to pump interactions with the lobes of the Ψ_{21} state superimposed on a background of stray light from the pump laser.

When the SAW is turned on, the intracavity trap becomes subjected to an effective modulation potential V_{SAW} given by [19]

$$V_{\text{SAW}}(x, t) = V_{\text{SAW},0} \cos(k_{\text{SAW}} x) \cos(\phi_{\text{SAW}}). \tag{3}$$

Here $k_{\text{SAW}} = 2\pi/\lambda_{\text{SAW}}$ and $\phi_{\text{SAW}} = 2\pi f_{\text{SAW}} t$ denote the wavevector and phase of the standing SAW field, respectively. Under the acoustic modulation, a signal–idler pair appears at energies equidistant to the pump energy, which thus signalizes OPO triggering. A detailed analysis of the dependence of the OPO excitation on the frequency of the rf drive applied to the IDT (cf. Supplement 1 Section 4) reveals that OPO states only appear for rf frequencies matching the modes of the acoustic resonator, which thus unambiguously proves that OPO triggering is induced by the SAW field.

The PL map of Fig. 2(d) also yields information about the symmetry of the confined states participating in the OPO process. In fact, the pump state in this figure has two lobes along x, which thus indicating that it corresponds to the Ψ_{21} state (rather than the closely lying Ψ_{12} state). The idler state, in contrast, has a single lobe along x located in between the two lobes of the pump state. This

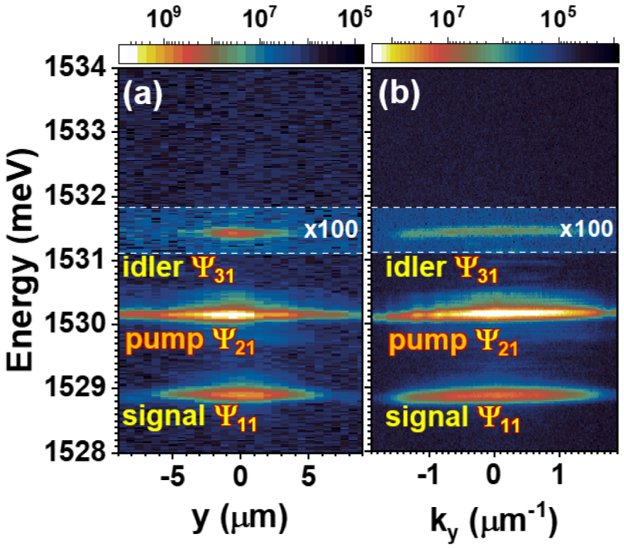

Fig. 3. OPO with resonant pump. Acoustically driven OPO detected by (a) spatially and (b) momentum-resolved PL. The PL maps were recorded along the direction y perpendicular to the SAW propagation axis x. The optical pump is in resonance to the Ψ_{21} level [cf. Fig. 2(a)] and triggers a type $O_3 = \{\Psi_{11}, \Psi_{21}, \Psi_{31}\}$ OPO.

emission pattern does not correspond to the one expected for the Ψ_{22} state but rather to a superposition of the state Ψ_{13} and Ψ_{31}. As will be shown in Section 4.A on acoustic modulation of confined levels, this state redshifts under the acoustic modulation to satisfy the OPO energy matching condition within the set of levels $O_2 = \{\Psi_{11}, \Psi_{21}, \Psi_{13}/\Psi_{31}\}$ displayed in the rightmost panels of Fig. 2.

Interestingly, the OPO level configuration is not unique and can be changed by varying the pump energy. Figure 3 displays PL maps recorded by setting the pump laser energy in resonance to the Ψ_{21} level (in contrast to the redshift pumping used in Fig. 2). The real-space and momentum-space (angle-resolved) maps were recorded in the direction orthogonal to the SAW propagation and optical excitation. While the OPO pump state is still Ψ_{21}, the idler has single emission maximum corresponding to the Ψ_{31} state. The excited OPO thus corresponds to $O_3 = \{\Psi_{11}, \Psi_{21}, \Psi_{31}\}$. We will show in Section 4.C on driven-dissipative simulations of the OPO dynamics that this OPO mode set is in full agreement with a numerical model for the OPO based on the Gross–Pitaevskii equation for this particular pump energy.

B. OPO Switching Dynamics

The dynamic character of the acoustic modulation was investigated by analyzing the time-dependent PL from the 4×4 μm intracavity trap. Figure 4(a) displays the PL response of polariton condensates in the first and the second confined levels recorded under SAW. This spectrum was acquired under nonresonant excitation at 1.54 eV with an optical power equal to twice the condensation threshold (P_{th}) [4]. The right panel compares the time-integrated PL spectra recorded in the absence of a SAW under weak optical excitation ($10^{-3}\ P_{\text{th}}$) and in the condensation regime ($2\,P_{\text{th}}$). The large energy blueshifts of the condensate energies with respect to the ones measured at low excitation are attributed to the polariton interactions with the excitonic reservoir produced by the nonresonant excitation. As discussed in detail in Ref. [19], the modulation by the SAW field leads to a sinusoidal dependence of the emission energy of the confined states.

The left panel in Fig. 4(b) shows the time-resolved emission of an OPO excited in the same trap by tuning the pump laser energy to the one from the second confined level at low excitation conditions (right panel). The signal blueshift in the OPO configuration is negligible compared to the one under the nonresonant excitation [cf. Fig. 4(a)] due to the absence of an excitonic reservoir. The emission from the signal and idler OPO states only appears during the restricted range of SAW phases for which these states are equidistant to the pump. The time trace confirms the dynamic nature of the acoustic tuning. The turn-on and turn-off times of the OPO (taken as the time delay for the intensity of the signal state to change by an order of magnitude) is below the temporal resolution of the present measurements of approximately 100 ps.

The OPO triggering dynamics depends on the SAW amplitude and phase as well as on the pump energy. Figure 5 illustrates different dynamic regimes that can be realized by varying the pump energy. At low pump energies, the OPO is normally excited only over a small range of SAW phases. Depending on the SAW amplitude and pump energy, the OPO can be triggered once in a SAW cycle, as in Figs. 5(a) and 5(b), or twice in a SAW cycle, as shown in Fig. 5(c). For high pump energies, the OPO can remain triggered over a range of SAW phases. The latter enables us to follow the dynamic energy modulation of the signal state induced by the SAW

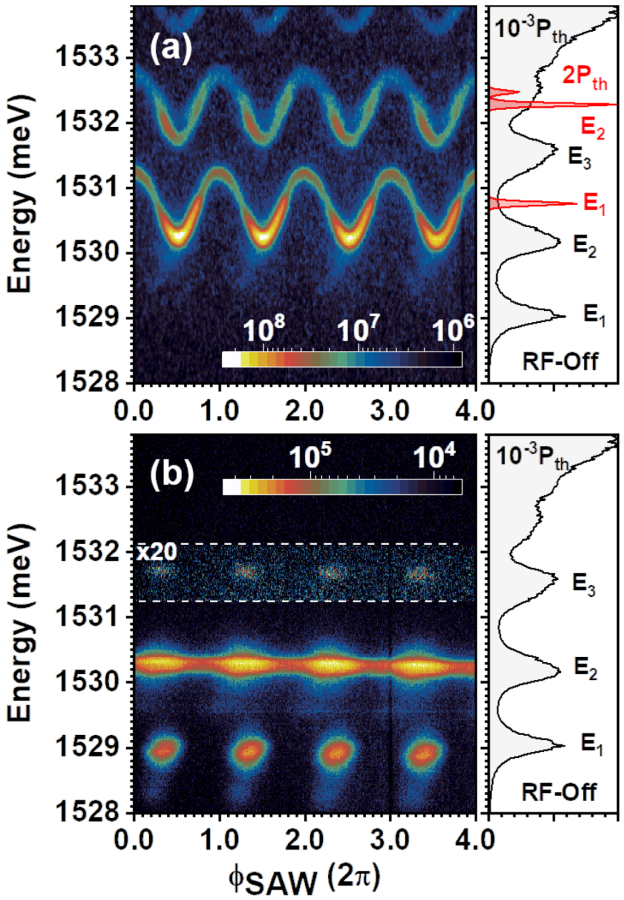

Fig. 4. Time-resolved OPO triggering. Time-resolved PL maps of the nominally 4×4 μm trap recorded under a $f_{SAW} = 383.69$ MHz SAW measured along the y axis perpendicular to the SAW direction. (a) Map acquired under nonresonant optical excitation with a power density $2P_{th}$, where P_{th} is the threshold power for the condensation. The right panel displays the spectral dependence of the time-integrated emission in the absence of a SAW for optical excitation powers of $10^{-3}P_{th}$ (black) and $2P_{th}$ (red). (b) OPO excitation by pumping the second confined level under the same acoustic excitation and comparable optical power as in (a). The right panel displays the integrated PL in the absence of a SAW for optical excitation powers of $10^{-3}P_{th}$. The phases in (a) and (b) were not synchronized and were aligned manually using the numerical simulations of Supplement 1.

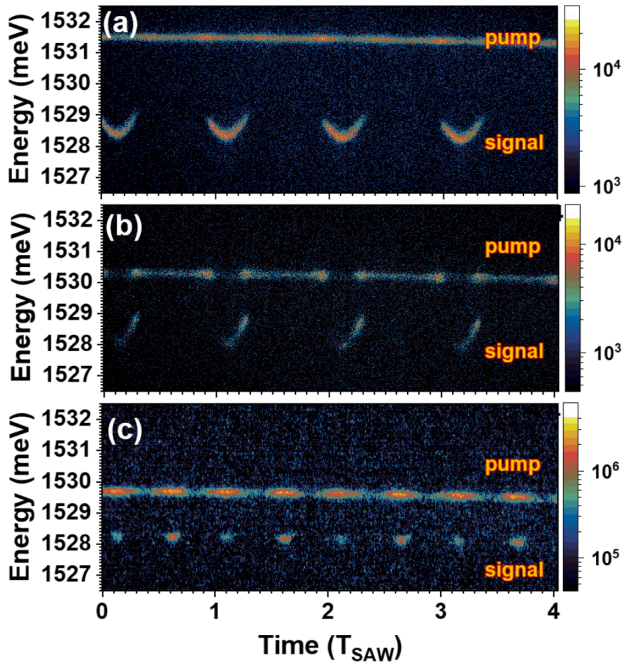

Fig. 5. OPO at different pump conditions. Time-resolved PL maps of an acoustically triggered OPO in a nominally 4×4 μm^2 trap excited by the pump with energies (a) 1531.5 meV, (b) 1530.3 meV, and (c) 1529.7 meV. Note that in (c) the OPO triggers twice in a SAW period (ss $T_{SAW} = 2.61$ ns).

field as illustrated in Figs. 5(a) and 5(b). Due to the relatively few accumulations, the idler signature is not visible. We note that in all cases, the signal energy for the OPO triggering is always slightly lower than the one for the OPO turn-off, which thus shows a hysteretic dependence on the SAW phase. This behavior is attributed to the dynamic energy shifts of the OPO states arising from polariton–polariton interactions. Once the OPO is triggered, the SAW-induced energy shifts of the OPO levels can be counteracted by changes in the polariton density due to the stimulated scattering to the signal and idler states. In this way, it becomes possible to fulfill the OPO energy conservation requirement for a range of SAW phases and energies of the pump state.

The OPO dynamics can be reproduced using a driven-dissipative theoretical framework augmented with the time-varying acoustic potential. Indeed, the theoretical prediction of the OPO triggering conditions and state symmetries [see Fig. 6(h)] are in excellent agreement with the experiment [cf. Fig. 3(b)]. The theoretical considerations are detailed in Section 4.C on driven-dissipative simulations of the OPO dynamics.

C. OPO Arrays

We now demonstrate that the acoustic triggering is very robust against fluctuations in trap size and energies, which thus makes it possible to synchronously trigger OPO in an array of traps. The studies were carried out in a square array of 3×3 μm^2 traps with a pitch of 9 μm shown in Fig. 7(a). Figure 7(b) displays a PL map, recorded under weak nonresonant excitation and in the absence of SAW by collecting the PL within the area indicated by the dashed rectangle in Fig. 7(a). The large spatial separation between the traps prevents tunnel coupling between them. The map thus reveals a series of confined states with almost identical energy spectrum for all traps. OPO experiment conditions are identical to the single 4×4 μm^2 trap discussed above. Figures 1(c) and 7(c) show the corresponding PL map obtained by pumping the array in resonance and slightly below the Ψ_{12} level, respectively, in the presence of the acoustic field. In both cases, OPOs are activated in all intracavity traps with correlated triggering times determined by the SAW phase at the trap location. Similar to the behaviour observed for a single trap [cf. Fig. 2(c)], no OPO excitation is observed in the absence of a SAW. The variations of the signal and idler energies on trap position arises from the Gaussian shape of the exciting laser beam, which populates the traps with different polariton densities. These fluctuations, however, do not prevent OPO triggering in all lattice sites under the acoustic modulation.

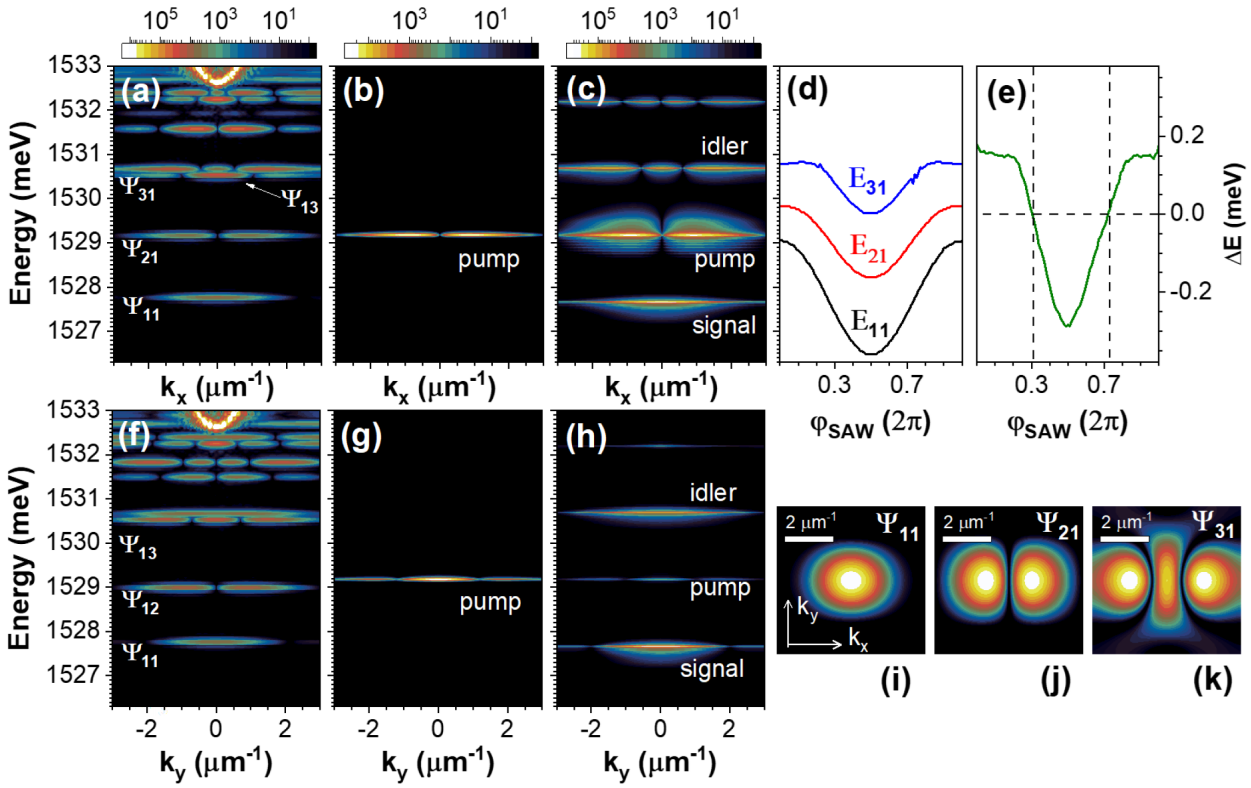

Fig. 6. Theoretical analysis of acoustically tuned OPOs. Numerical simulations carried out by solving the driven-dissipative Gross–Pitaevskii equation for polaritons in an 4×4 μm^2 intracavity trap. (a) and (f) Momentum-space spectra of the trap along the x and y directions, respectively, under nonresonant excitation and in the absence of SAW. (b) and (g) Momentum-space spectra of the trap under resonant excitation into Ψ_{21} state in the absence of SAW along the x and y directions, respectively. (c) and (h) Similar to (b) and (g) but for the SAW phase of 0.3 in units of 2π. (d) Evolution of the energy of the OPO levels over one SAW cycle. (e) Energy difference $\Delta E = E_{31} + E_{11} - 2E_{21}$ between the Ψ_{ij} levels over one SAW period. The vertical dashed lines designate two SAW phases for which the spectrum of the trap is equidistant ($\Delta E = 0$). (i)–(k) Spatial profiles of the squared wave functions of the signal, pump, and idler states at SAW phase of $0.3(2\pi)$.

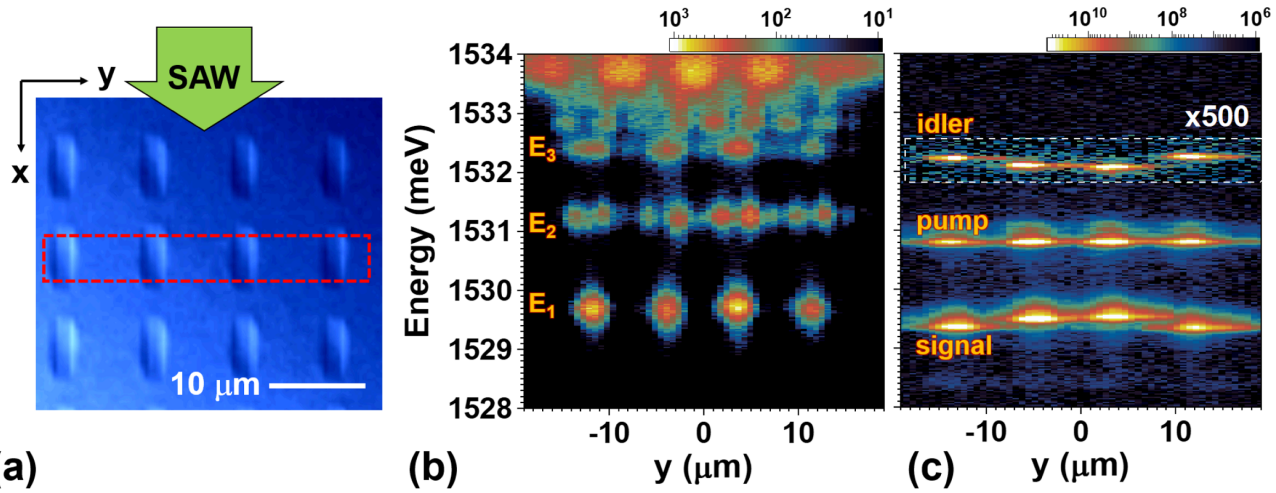

Fig. 7. Arrays of acoustically tuned OPOs. (a) An optical micrograph of an array of nominally 3×3 μm^2 intracavity traps with a pitch of 9 μm. The dashed rectangle designates the region probed by PL. (b)–(c) Spectral PL maps of the array recorded (a) under weak nonresonant excitation in the absence of SAW and (b) strong (power comparable to Fig. 4) resonant excitation in the presence of SAW.

4. DISCUSSION

In the following we address the theoretical framework and explain the results of the previous sections. We start with a simple model for the effects of the spatially varying SAW fields on the confined polariton states, which gives quantitative insights into the mechanisms for the state-dependent modulation of the confined levels as well as the symmetry of the OPO states. We then proceed with numerical simulations of the driven-dissipative OPO dynamics, which are in agreement with the previous model and reproduce very well the observed OPO behavior. Finally, we address the

intensity ratio between the idler and signal PL, which depends on the decay rate of the corresponding polariton states and is a relevant parameter for the generation of correlated photons.

A. Acoustic Modulation of Confined Levels

The state-dependent acoustic energy tuning mainly relies on the SAW strain field. The latter modulates the excitonic component of polaritons via the deformation potential mechanism as well as the photonic component due to modulation of the thickness and refractive index of the MC layers [20,21]. These two modulation mechanisms add in phase for the present sample and lead to the effective standing potential for polaritons given by Eq. (3).

The symmetry and time evolution of the polariton levels under a standing acoustic field can be understood by using perturbation theory to calculate the impact of the dynamical potential V_{SAW} [cf. Eq. (3)] on the confined levels given by Eq. (1). The acoustically induced energy shifts of the $\Psi_{m_x m_y}$ can be expressed as (see Supplement 1 Section 3 for details)

$$\Delta E_{m_x m_y} = \langle \Psi_{m_x m_y} | \phi_{\mathrm{SAW}} | \Psi_{m_x m_y} \rangle \approx V_{\mathrm{SAW},0} \left(\frac{\pi^2}{6} - \frac{1}{m_x^2} \right) \left(\frac{l_x}{\lambda_{\mathrm{SAW}}} \right)^2 \cos(\phi_{\mathrm{SAW}}). \quad (4)$$

The acoustic modulation thus introduces a spatial distortion of the confinement potential, which depends on the instantaneous amplitude $V_{\mathrm{SAW},0}\cos(\phi_{\mathrm{SAW}})$ of the standing field as well as the ratio of the trap dimensions to the acoustic wavelength. The corresponding energy shifts $\Delta E_{m_x m_y}$ are independent of the mode index m_y but reduce with increasing m_x. This behavior arises from the fact that the m_y lobes of the wave function are centered on the SAW antinodes, which thus experience the full strain-induced energy modulation. In contrast, the m_x lobes are oriented along the SAW propagation direction and, therefore, probe different phases of the standing SAW field.

These state-dependent shifts enable the dynamic energy tuning for OPO triggering over a wide range of trap geometries (see Supplement 1 Section 3). In particular, the OPO states $O_2 = \{\Psi_{11}, \Psi_{21}, \Psi_{31}\}$ in a perfect square trap become equidistant in energy by selecting the SAW amplitude and phase to satisfy

$$V_{\mathrm{SAW},0}\cos(\phi_{\mathrm{SAW}}) = \frac{2}{3}\left(\frac{\lambda_{\mathrm{SAW}}}{\ell} \right)^2. \quad (5)$$

In order to determine the nature of the OPO states, we first examine the impact of the SAW on the energy of the states given by Eq. (3). Figure 2(e) displays the energy evolution of the confined polariton levels with the SAW phase ϕ_{SAW}. The calculations were carried out using a numerical approach that takes into account the measured spatial profile of the traps (see Supplement 1 for details) but neglects polariton interactions. A more realistic model taking into account the interactions will be discussed further. The vertical dash-dotted black lines mark the nodes of the SAW strain field, where the polariton states are identical to those of an unperturbed trap. The states within the set $O_1 = \{\Psi_{11}, \Psi_{12}\mathrm{or}\Psi_{21}, \Psi_{22}\}$ are approximately equidistant for this phase, but, for symmetry reasons outlined below, do not interact to form an OPO even under a SAW. The vertical dashed blue lines indicate the phases for which the OPO energy matching requirement is satisfied for the set $O_2 = \{\Psi_{11}, \Psi_{21}, \Psi_{31}/\Psi_{13}\}$. We attribute the PL features in Fig. 2(d) to an OPO involving these states. This assignment is supported by a comparison of the PL maps with their calculated squared wave function $|\Psi_{m_x m_y}|^2$, displayed in Figs. 2(f)–2(h), for the matching SAW phase. The pump state has thus a predominantly Ψ_{21} character with two lobes along x. The idler state results from the SAW-induced redshift of the Ψ_{13} unperturbed state, which mixes with the Ψ_{31} state. The idler state thus acquires the symmetry shown in Fig. 2(f).

When the pump energy is in resonance or blueshifted with respect to the Ψ_{21} state, the OPO acquires the O_3 configuration (cf. Fig. 3) with the Ψ_{31} idler state.

B. Symmetry of the OPO States

Previous sections have shown that acoustic tuning enables the excitation of OPO in intracavity traps over a wide range of optical and acoustical excitation conditions. One interesting question is why it is not possible to trigger an OPO in the configuration $O_1 = \{\Psi_{11}, \Psi_{21}(\mathrm{or}\ \Psi_{12}), \Psi_{22}\}$, which has equally separated states for a perfect square potential. In fact, we show (Supplement 1 Section 3) that deviations from a square shape can also be corrected by the acoustic field. The required field amplitudes are in this case much smaller than those given by Eq. (5) for the energy matching of the O_2 states.

The inability to excite an O_1 OPO arises from symmetry requirements of the nonlinear process responsible for OPO triggering, a critical process to initiate parametric oscillations. OPO triggering initiates when fluctuations of the polariton population lead to the occupation of the pump state by two polaritons. The latter process creates a nonadiabatic and nonlinear potential that couples the initial two-polariton state $\{\Psi_p \Psi_p\}$ to the final state $\{\Psi_s \Psi_i\}$ consisting of particles in a superposition of signal and idler states. In the contact approximation for polariton–polariton interactions [22,23], the perturbed two-polariton state represented by $\{\Psi_p \Psi_p\}'$ can be expressed as

$$\{\Psi_p \Psi_p\}' \approx \{\Psi_p \Psi_p\} + \frac{\langle \{\Psi_s \Psi_i\} | \delta V_p | \{\Psi_p \Psi_p\} \rangle}{2(E_p - E_s)} \{\Psi_s \Psi_i\} + \ldots. \quad (6)$$

The coupling Hamiltonian δV_p can be expressed as

$$\delta V_p = \int g \left[\Psi_i \Psi_s \Psi_p^2 \right] \mathrm{d}x \mathrm{d}y, \quad (7)$$

where g denotes the effective polariton–polariton coupling strength. The nonlinear coupling δV_p thus enables the scattering of pump polaritons to the idler and signal states required to trigger the stimulated scattering, leading to parametric oscillations and amplification.

Equation (7) has important consequences for potentials with mirror symmetry, such as the ones studied here. The confined states Ψ_{ij} in these potentials have a well-defined parity. Since $|\Psi_p|^2$ in Eq. (7) is always an even function, a nonvanishing coupling δV_p requires idler and signal states with the same parity, i.e., states with indices m_i $(i = x, y)$ differing by an even number. This condition is satisfied for the sets O_2 and O_3 but not for O_1, in full agreement with the experimental results.

The previously mentioned symmetry requirements remain valid under a standing SAW field, as long as the traps are centered at a field antinode, since in this case the acoustic perturbation does not affect the mirror symmetry of the trap potential. However, if the SAW field has a traveling component (or if the trap is displaced

from the antinodes of a standing field), it will mix states with different parities and enable other OPO configurations.

C. Driven-Dissipative Simulations of the OPO Dynamics

In the following we present a theoretical analysis based on the numerical solution of the driven-dissipative Gross–Pitaevskii equation (GPE) for the lower-polariton field (Ψ) in an intracavity trap subjected to an optical field [$(F_p(\mathbf{r}, t)$ with $\mathbf{r} = (x, y)$] as well as to the acoustic modulation potential given by Eq. (3). In contrast to the single-particle calculations presented above, the GPE solutions implicitly account for the polariton nonlinearity leading to the OPO formation. In atomic units, the GPE can be expressed as

$$i\partial_t \Psi(\mathbf{r}, t) = F_p(\mathbf{r}, t) + (\omega_{\mathrm{LP}}(-i\nabla) - i\kappa_{\mathrm{LP}} + g_{\mathrm{LP}}|\Psi(\mathbf{r}, t)|^2 + V_{\mathrm{trap}}(\mathbf{r}) + V_{\mathrm{SAW}}(\mathbf{r}, t))\,\Psi(\mathbf{r}, t). \tag{8}$$

Here ω_{LP}, κ_{LP}, and g_{LP} are lower-polariton dispersion, decay rate, and polariton–polariton interaction constant, respectively. The dimensions of the intracavity trap were determined from AFM height maps; see Table S1 of Supplement 1. The parameters for the trap potential and the SAW modulation amplitude were the same as in the experiments. Details of the calculations procedure are summarized in Supplement 1 Section 6.

Figures 6(a) and 6(f) display the wave function projections of the polariton states (in momentum space) calculated for low-power, nonresonant optical excitation of the trap. The central panels [Figs. 6(b) and 6(g)] show the corresponding maps under polariton injection into the Ψ_{21} state, which blueshifts due to the polariton–polariton interactions. In agreement with the experimental results in the absence of SAW, no OPO is observed under these conditions. In contrast, once the SAW potential is added, the signal and idler states appear in the simulated spectra [cf. Figs. 6(c) and 6(h)]. We emphasize here the excellent agreement between the calculated energies and wave function projections of Fig. 6(h) with the experimentally determined energies and momentum-resolved PL maps of Fig. 3(b). Note, however, that the complexity of the processes governing polariton dephasing and decay into photons makes it difficult to relate the polariton wave functions in Fig. 6 to the intensities of the measured PL maps.

The wave functions of the OPO states illustrated in Figs. 6(i)–6(k) correspond to the ones expected for an OPO involving the set $O_3 = \{\Psi_{11}, \Psi_{21}, \Psi_{31}\}$. The dependence of their energy on the SAW phase, which is summarized in Figs. 6(d) and 6(e), shows that the OPO energy matching conditions are satisfied twice in a SAW cycle for $\phi_{\mathrm{SAW}} = 0.3$ and 0.7 rad.

D. Idler–Signal Intensities Ratio

We use the ratio of the combined intensities of the signal and idler modes to the total intensity of the OPO states, including the scattered light from the pump state, as an estimate of the OPO efficiency. Indeed, the amount of light scattered at the pump energy [as directly measured, for instance, in Fig. 1(c)] is proportional to the polariton density at that energy. Therefore, the OPO efficiency (η_{OPO}) for a single trap can be estimated from the Fig. 1(c) as $\eta_{\mathrm{OPO}} = (I_s + I_i)/I_{\mathrm{total}} \times 100$, where $I_{\mathrm{total}} = I_p + I_s + I_i$ is the total OPO intenisty and $I_{s/i/p}$ are signal/idler/pump integrated intensities. The integrated PL intensity of the second trap from the left is shown in Fig. 1(d). For this trap we obtain $\eta_{\mathrm{OPO}} = 57\%$. The value is only the lower limit estimate, due to the fact that the collection efficiency depends on the mode symmetry (angular distribution of emission).

In the following, we discuss the discrepancy between signal and idler efficiencies. The OPO process yields pairs of signal and idler polaritons: the same applies for the simulation of Figs. 6(c), 6(h) that predicts almost identical amplitudes for the signal and idler states. The PL yield from these states depends on how the polaritons decay to photons and may differ considerably due to differences in the scattering rates, Hopfield coefficients, emission pattern, and photon reabsorption. As a result, the emission from idler states is normally much weaker than that from the signal. The latter is a main drawback for applications as sources of correlated photons, which ideally require comparable intensity ratios for signal and idler.

The ratio r_{OPO} between the integrated emission intensity of the signal and idler in the present studies covers a wide range extending from 20 to 500. For comparison, the OPOs based on confined polariton states reported in Ref. [15] have r_{OPO} ratios ranging from approximately 5 to 100, depending on the excitation intensity, which compares with the range from 5 to 10 predicted by theoretical studies presented in the same work. The disparity increases to 10^3 to 10^4 in polariton OPOs based on triple microcavities [13].

The high value of r_{OPO} inferred from Figs. 1 and 2 is partially due to an inefficient collection of the idler emission. In fact, the emission in the PL maps will appear very weak if the idler state has a spatially extended wave function or, as discussed in Section 3.A on SAW-induced OPO, an emission node along the collection axis. We estimate that the limited collection of the idler emission, which can be eliminated by a full measurement of the wave functions, results in an increase of the measured r_{OPO} by a factor between 3 and 5.

Another mechanism leading to the large r_{OPO} arises from the higher photonic content of the signal state in comparison to the idler state in the present sample. However, the energy difference between signal and idler states is less than half of the Rabi splitting, so the large r_{OPO} ratios cannot be solely attributed to differences in the Hopfield coefficients.

Lastly, the large value of r_{OPO} may also arise from decay paths from the pump to the low-lying signal states (e.g., by a thermal process). Figure 2(d) shows, however, that the signal state only emits under OPO excitation, which thus proves the absence of a parallel decay path. We suggest that the weak photon yield of the idler results from the strong dephasing arising from the coupling with closely lying energy levels. The acoustic field may play a role in this process: in particular, the SAWs applied here also carry piezoelectric fields, which interact strongly and can efficiently mix electronic states. Future studies using nonpiezoelectric SAWs [24] will help to clarify this issue.

5. CONCLUSION

We have demonstrated an efficient and versatile approach for the dynamic control of the scattering pathways of confined polaritons based on modulation by spatially and time-varying potentials produced by megahertz SAWs. A unique feature arising from the spatial dependence of the SAW field is the ability to dynamically control the energy of individual polariton states in a confined potential. Here the SAW is applied to tune the energy states of

confined polaritons to enable OPO. We demonstrated that the acoustic OPO requires not only the matching of the energy-level separation, but also signal, pump, and idler states with the appropriate symmetry. The experimental studies have been complemented by a theoretical framework, which accounts for the required symmetry of the confined states and also provides a quantitative determination of the energy tuning parameters. We have demonstrated that the dynamic character and the robust nature of the acoustic tuning enables OPOs over a wide range of excitation conditions.

The ability to synchronously enable multiple OPOs is another advantage of our approach. This functionality has been demonstrated by the excitation of an array of confined OPOs using a single acoustic beam. The modulation of the individual polariton traps of the array tunes the energy of the confined levels and counteracts unavoidable energy fluctuations. Furthermore, the OPO emission from the array sites is correlated by the SAW phase. The signal–idler photon pairs are emitted not only at well-defined locations within the array but also at well-determined times, a feature which can enhance the fidelity of such a source of correlated photons. The time jitter of the emission due to the fluctuations in the trap properties could be minimized by increasing the SAW amplitude.

A natural future step will be the exploitation of acoustically tuned OPOs for the generation of entangled photons from a single trap and arrays. We anticipate that one of the challenges will be to minimize the mismatch in emission intensity between the signal and idler states. The theoretical framework together with the ability to design polariton confinement potentials with the appropriate symmetry are an excellent starting point to reach this goal.

As a final remark, we point out that strain fields interact with a wide variety of excitations in solid-state systems [25]. The reported dynamical acoustic tuning can be applied to a wide variety of systems, which therefore provides the robustness in operation required for the realization of scalable on-chip systems.

Funding. Engineering and Physical Sciences Research Council (EP/R04399X/1); Deutsche Forschungsgemeinschaft (359162958); Bundesministerium für Bildung und Forschung (13N14783).

Acknowledgment. The authors thank M. Ramsteiner and S. Krishnamurthy for discussions and for a critical review of the manuscript. We also acknowledge the technical support from R. Baumann, S. Rauwerdink, and A. Tahraoui in the sample fabrication process.

Disclosures. The authors declare no conflicts of interest.

See Supplement 1 for supporting content.

REFERENCES

1. C. Weisbuch, M. Nishioka, A. Ishikawa, and Y. Arakawa, "Observation of the coupled exciton-photon mode splitting in a semiconductor quantum microcavity," Phys. Rev. Lett. **69**, 3314–3317 (1992).
2. I. Carusotto and C. Ciuti, "Quantum fluids of light," Rev. Mod. Phys. **85**, 299–366 (2013).
3. D. Sanvitto and S. Kena-Cohen, "The road towards polaritonic devices," Nat. Mater. **15**, 1061–1073 (2016).
4. J. Kasprzak, M. Richard, S. Kundermann, A. Baas, P. Jeambrun, J. M. J. Keeling, F. M. Marchetti, M. H. Szymańska, R. André, J. L. Staehli, V. Savona, P. B. Littlewood, B. Deveaud, and L. S. Dang, "Bose-Einstein condensation of exciton polaritons," Nature **443**, 409–414 (2006).
5. J. J. Baumberg, P. G. Savvidis, R. M. Stevenson, A. I. Tartakovskii, M. S. Skolnick, D. M. Whittaker, and J. S. Roberts, "Parametric oscillation in a vertical microcavity: a polariton condensate or micro-optical parametric oscillation," Phys. Rev. B **62**, 16247–16250 (2000).
6. M. Saba, C. Ciuti, J. Bloch, V. Thierry-Mieg, R. André, S. S. Dang, S. Kundermann, A. Mura, G. Bongiovanni, J. L. Staehli, and B. Deveaud, "High-temperature ultrafast polariton parametric amplification in semiconductor microcavities," Nature **414**, 731–735 (2001).
7. W. Langbein, "Spontaneous parametric scattering of microcavity polaritons in momentum space," Phys. Rev. B **70**, 205301 (2004).
8. P. G. Savvidis, J. J. Baumberg, R. M. Stevenson, M. S. Skolnick, D. M. Whittaker, and J. S. Roberts, "Angle-resonant stimulated polariton amplifier," Phys. Rev. Lett. **84**, 1547–1550 (2000).
9. C. Ciuti, "Branch-entangled polariton pairs in planar microcavities and photonic wires," Phys. Rev. B **69**, 245304 (2004).
10. S. Savasta, O. D. Stefano, V. Savona, and W. Langbein, "Quantum complementarity of microcavity polaritons," Phys. Rev. Lett. **94**, 246401 (2005).
11. M. Romanelli, C. Leyder, J. P. Karr, E. Giacobino, and A. Bramati, "Four wave mixing oscillation in a semiconductor microcavity: generation of two correlated polariton populations," Phys. Rev. Lett. **98**, 106401 (2007).
12. S. Portolan, O. D. Stefano, S. Savasta, and V. Savona, "Emergent entanglement of microcavity polariton pairs," J. Phys. Conf. Ser. **210**, 012033 (2010).
13. C. Diederichs, J. Tignon, G. Dasbach, C. Ciuti, A. Lemaître, J. Bloch, P. Roussignol, and C. Delalande, "Parametric oscillation in vertical triple microcavities," Nature **440**, 904–907 (2006).
14. C. Schneider, K. Winkler, M. D. Fraser, M. Kamp, Y. Yamamoto, E. A. Ostrovskaya, and S. Höfling, "Exciton-polariton trapping and potential landscape engineering," Rep. Prog. Phys. **80**, 016503 (2017).
15. L. Ferrier, S. Pigeon, E. Wertz, M. Bamba, P. Senellart, I. Sagnes, A. Lemaître, C. Ciuti, and J. Bloch, "Polariton parametric oscillation in a single micropillar cavity," Appl. Phys. Lett. **97**, 031105 (2010).
16. N. C. Zambon, S. R. K. Rodriguez, A. Lemaitre, A. Harouri, L. L. Gratiet, I. Sagnes, P. St-Jean, S. Ravets, A. Amo, and J. Bloch, "Parametric instability in coupled nonlinear microcavities," Phys. Rev. A **102**, 023526 (2020).
17. C. Ozanam, M. Savanier, L. Lanco, X. Lafosse, G. Almuneau, A. Andronico, I. Favero, S. Ducci, and G. Leo, "Toward an AlGaAs/AlO_x near-infrared integrated optical parametric oscillator," J. Opt. Soc. Am. B **31**, 542–550 (2014).
18. A. S. Kuznetsov, P. L. J. Helgers, K. Biermann, and P. V. Santos, "Quantum confinement of exciton-polaritons in structured (Al, Ga)As microcavity," Phys. Rev. B **97**, 195309 (2018).
19. A. S. Kuznetsov, K. Biermann, and P. V. Santos, "Dynamic acousto-optical control of confined polariton condensates: from single traps to coupled lattices," Phys. Rev. Res. **1**, 023030 (2019).
20. T. Sogawa, P. V. Santos, S. K. Zhang, S. Eshlaghi, A. D. Wieck, and K. H. Ploog, "Dynamic band-structure modulation of quantum wells by surface acoustic waves," Phys. Rev. B **63**, 121307 (2001).
21. M. M. de Lima, Jr. and P. V. Santos, "Modulation of photonic structures by surface acoustic waves," Rep. Prog. Phys. **68**, 1639–1701 (2005).
22. C. Ciuti, P. Schwendimann, and A. Quattropani, "Parametric luminescence of microcavity polaritons," Phys. Rev. B **63**, 041303 (2001).
23. I. Carusotto and C. Ciuti, "Spontaneous microcavity-polariton coherence across the parametric threshold: quantum Monte Carlo studies," Phys. Rev. B **72**, 125335 (2005).
24. J. Rudolph, R. Hey, and P. V. Santos, "Long-range exciton transport by dynamic strain fields in a GaAs quantum well," Phys. Rev. Lett. **99**, 047602 (2007).
25. P. Delsing, A. N. Cleland, M. J. A. Schuetz, J. Knörzer, G. Giedke, J. I. Cirac, K. Srinivasan, M. Wu, K. C. Balram, C. Bäuerle, T. Meunier, C. J. B. Ford, P. V. Santos, E. Cerda-Méndez, H. Wang, H. J. Krenner, E. D. S. Nysten, M. Weiß, G. R. Nash, L. Thevenard, C. Gourdon, P. Rovillain, M. Marangolo, J.-Y. Duquesne, G. Fischerauer, A. Reiner, B. Paschke, D. Denysenko, D. Volkmer, A. Wixforth, H. Bruus, M. Wiklund, J. Reboud, J. M. Cooper, Y. Fu, M. S. Brugger, F. Rehfeldt, and C. Westerhausen, "The 2019 surface acoustic waves roadmap," J. Phys. D **52**, 353001 (2019).